



HAL
open science

Composition and morphology of self-organized Mn-rich nanocolumns embedded in Ge: Correlation with the magnetic properties

I. Mouton, Rodrigue Lardé, Etienne Talbot, E. Cadel, C. Genevois, D. Blavette, V. Baltz, E. Prestat, Pascale Bayle-Guillemaud, A. Barski, et al.

► To cite this version:

I. Mouton, Rodrigue Lardé, Etienne Talbot, E. Cadel, C. Genevois, et al.. Composition and morphology of self-organized Mn-rich nanocolumns embedded in Ge: Correlation with the magnetic properties. *Journal of Applied Physics*, 2012, 112 (11), pp.113918. 10.1063/1.4768723 . hal-01633477

HAL Id: hal-01633477

<https://hal.science/hal-01633477>

Submitted on 28 Feb 2019

HAL is a multi-disciplinary open access archive for the deposit and dissemination of scientific research documents, whether they are published or not. The documents may come from teaching and research institutions in France or abroad, or from public or private research centers.

L'archive ouverte pluridisciplinaire **HAL**, est destinée au dépôt et à la diffusion de documents scientifiques de niveau recherche, publiés ou non, émanant des établissements d'enseignement et de recherche français ou étrangers, des laboratoires publics ou privés.

Composition and morphology of self-organized Mn-rich nanocolumns embedded in Ge: Correlation with the magnetic properties

I. Mouton, R. Lardé, E. Talbot, E. Cadel, C. Genevois et al.

Citation: *J. Appl. Phys.* **112**, 113918 (2012); doi: 10.1063/1.4768723

View online: <http://dx.doi.org/10.1063/1.4768723>

View Table of Contents: <http://jap.aip.org/resource/1/JAPIAU/v112/i11>

Published by the [American Institute of Physics](#).

Related Articles

Magnetocaloric properties of La(Fe,Si)₁₃-based material and its hydride prepared by industrial mischmetal
Appl. Phys. Lett. **101**, 162406 (2012)

Reversible ferromagnetism in rutile TiO₂ single crystals induced by nickel impurities
Appl. Phys. Lett. **101**, 142105 (2012)

Spin stability and magnetic screening of a magnetic impurity in four-terminal Landauer setup with Rashba spin-orbit coupling
J. Appl. Phys. **111**, 07C324 (2012)

Spin-current switch based on vertical asymmetric double quantum dots containing single manganese
J. Appl. Phys. **111**, 07C320 (2012)

Spin dynamics in the multiferroic materials (invited)
J. Appl. Phys. **111**, 07E137 (2012)

Additional information on J. Appl. Phys.

Journal Homepage: <http://jap.aip.org/>

Journal Information: http://jap.aip.org/about/about_the_journal

Top downloads: http://jap.aip.org/features/most_downloaded

Information for Authors: <http://jap.aip.org/authors>

ADVERTISEMENT



AIP Advances

Now Indexed in
Thomson Reuters
Databases

Explore AIP's open access journal:

- Rapid publication
- Article-level metrics
- Post-publication rating and commenting

Composition and morphology of self-organized Mn-rich nanocolumns embedded in Ge: Correlation with the magnetic properties

I. Mouton,¹ R. Lardé,^{1,a)} E. Talbot,¹ E. Cadel,¹ C. Genevois,¹ D. Blavette,¹ V. Baltz,² E. Prestat,^{3,4} P. Bayle-Guillemaud,⁴ A. Barski,⁴ and M. Jamet⁴

¹Groupe de Physique des Matériaux, UMR CNRS 6634, Université et INSA de Rouen, Avenue de l'Université, BP 12, 76801 St Etienne du Rouvray, France

²SPINTEC, UMR CEA/CNRS/UJF-Grenoble 1/Grenoble-INP, INAC, 38054 Grenoble, France

³Karlsruhe Institut für Technologie (KIT), Laboratorium für Elektronenmikroskopie, D-76128 Karlsruhe, Germany

⁴INAC/SP2M CEA-Grenoble et Université Joseph Fourier, 38054 Grenoble, France

(Received 18 July 2012; accepted 7 November 2012; published online 12 December 2012)

The morphology and composition of self organized manganese (Mn)-rich nanocolumns embedded in germanium (Ge) thin films were characterized at the atomic scale and in three dimensions with high resolution transmission electron microscopy and atom probe tomography. Experiments revealed Mn-enriched nano-columns of 3 nm in diameter with various morphologies. Their Mn-content was found smaller than that of the expected equilibrium phases and chemical fluctuations along the growth axis were additionally observed. By contrast, less than 0.05% of Mn was measured in the Ge-matrix. These results were correlated to the magnetic properties and allowed understanding the magnetic behavior of the nanocolumns. © 2012 American Institute of Physics. [<http://dx.doi.org/10.1063/1.4768723>]

I. INTRODUCTION

The search for future spintronic devices compatible with silicon technology has motivated many studies on ferromagnetic semiconductors. Diluted magnetic semiconductors (DMSs) were first believed as the most promising materials.¹ In such materials, transition metal (TM) magnetic atoms are randomly dispersed in a semiconducting host matrix. DMS are close to materials used in microelectronics and show simultaneously semiconducting and ferromagnetic properties.² However, nowadays well-controlled DMS based on II-VI and III-V semiconductors still have very low Curie temperature (T_C), which constitutes the main obstacle for practical applications. Although some groups have reported room temperature ferromagnetism in some DMS systems, its origin is still unclear and remains a matter of intense debate.³ In heavily TM doped magnetic semiconductors, it is now admitted that the magnetic and magneto-transport properties may be attributed to the uncontrolled formation of nanosized TM-rich regions.⁴ Initially, these chemical inhomogeneities were considered undesirable. They are now foreseen as a way to produce devices with higher T_C .⁵ Indeed, the presence of magnetically active zones can increase the critical temperature and lead to enhanced magnetotransport and magneto-optical properties. Such inhomogeneous magnetic semiconductors could pave the way for a variety of novel applications (i.e., magnetic memories, magnetic sensors, and spintronic devices).^{6,7} Among these systems, Mn-doped Ge has attracted particular attention and several studies^{8–17} have already been carried out. It was shown that Mn rich precipitates can be formed in a Ge matrix depending on the Mn concentration and growth conditions. Equilibrium Ge_3Mn_5 and

$\text{Ge}_8\text{Mn}_{11}$ phases or unstable Mn-rich nanostructures (i.e., tadpoles¹⁶ or self organized nanocolumns¹¹) were reported. In this context, the precise characterisation and control of the nanostructure as well as a deeper understanding of nucleation and growth process and links with magnetism is as a challenge. Therefore, a detailed investigation at the ultimate length scale becomes crucial. Although Ge-Mn materials were widely characterized by high resolution electron transmission microscopy (HRTEM) and chemically analyzed by energy dispersive spectrometry (EDS) and electron energy-loss spectroscopy (EELS), there is still a lack of information about (i) the spatial distribution of Mn atoms and (ii) the chemical composition of inhomogeneities. In this paper, we have used HRTEM and atom probe tomography (APT) in a complementary way in order to bring additional information on the morphology and composition of self organized Mn-rich nanocolumns in Ge-Mn thin films. Subsequent new and refined correlations to the magnetic properties were suggested. APT is the only three dimensional (3D) analytical microscope able to map out the distribution of atoms at the atomic-scale.^{18,19} APT is therefore a unique approach to investigate phase transformations at the sub-nanoscale. Few APT experiments dealing with magnetic semiconductors were reported. Let us mention those on GaMnAs,²⁰ Cr-doped In_2O_3 ,²¹ and Co-doped ZnO.^{22–24} Results on Ge-Mn individual and stacked clusters and on co-doped Ge-(Mn,Co) thin films were also published by Bougeard *et al.*¹³ and Riley *et al.*,¹⁴ respectively.

II. EXPERIMENTAL PROCEDURE

A Ge-Mn thin film containing ~10 at. % Mn was grown by molecular beam epitaxy on a Ge (001) substrate. A 13 nm thick Ge buffer was first grown after thermal desorption of the native oxide. Ge and Mn atoms were subsequently

^{a)}Author to whom correspondence should be addressed. Electronic mail: rodrigue.larde@univ-rouen.fr.

co-evaporated in order to obtain an 80 nm thick $\text{Ge}_{0.9}\text{Mn}_{0.1}$ layer. The growth temperature was set to $\sim 100^\circ\text{C}$ and the growth rate was $\sim 0.02\text{ nm/s}$. In a previous work, it was shown that these growth conditions lead to an inhomogeneous distribution of Mn atoms and to the formation of pseudocrystalline Mn-rich nanocolumns finely dispersed in Ge matrix.¹¹ The film grown was first investigated through HRTEM at 200 kV by using both a JEOL ARM 200F microscope (probe cs-corrected) and a FEI-Titan 80–300 kV (probe and image cs-corrected) microscope and then analysed using a laser assisted wide angle tomographic atom probe (LAWATAP-CAMECA). TEM cross-section lamella and APT specimens (sharp tips) were prepared by lift-out method and standard milling²⁵ using a dual beam ZEISS Nvision 40. In order to reduce Ga implantation and to avoid damages in the region of interest, the $\text{Ge}_{0.9}\text{Mn}_{0.1}$ thin film was capped with 500 nm of Pt and a final polishing was performed at low acceleration voltage (2 kV). Chemical mechanical wedge polishing was used for TEM plane view lamella. For APT experiments, specimens were cooled at 80 K and field evaporated using 350 fs laser pulses (wavelength: $\lambda = 342\text{ nm}$). The principle of APT is based on the elemental identification of field evaporated ions by time of flight spectrometry. A position sensitive detector provides the location of surface atoms. The volume analysed, which is field evaporated layer by layer, is subsequently reconstructed in 3D. The magnetic properties have been investigated by using SQUID magnetometry with a magnetic field applied in the sample plane.

III. RESULTS

A. Structural and chemical characterization

Figures 1(a) and 1(b) show TEM cross section views of the $\text{Ge}_{0.9}\text{Mn}_{0.1}$ thin film. The images were taken in scanning mode at low angle annular dark field (STEM-LAADF) and in classical TEM mode, respectively. Note that the bright contrast observed in Figure 1(a) corresponds to the dark contrast in Figure 1(b). The Ge buffer layer and the $\text{Ge}_{0.9}\text{Mn}_{0.1}$ thin film are clearly observed. The Ge-buffer/Ge-substrate interface is revealed by a lighter line which corresponds to the initial prepared surface of the Ge substrate. Vertical inhomogeneities running over the whole film are clearly distinguished. Energy filtering images (not shown here) correlate these inhomogeneities to the presence of Mn-rich nanocolumns embedded in a Mn-poor Ge matrix. Figures 1(c) and 1(d) show a plane view of the $\text{Ge}_{0.9}\text{Mn}_{0.1}$ layer obtained by STEM bright field (BF) and annular dark field (ADF), respectively. This shows the spatial distribution of the nanocolumns. The two reversed contrasts are complementary and underline the features of the columns in projection and along the growth direction. The high resolution imaging reveals that they are not fully crystalline.

Figures 2(a) and 2(b) show TEM cross section views of the $\text{Ge}_{0.9}\text{Mn}_{0.1}$ thin film in high resolution mode (HRTEM). The HRTEM images show that the $\text{Ge}_{0.9}\text{Mn}_{0.1}$ layer and the buffer layer are in perfect epitaxial match with the Ge substrate. We clearly observe the presence of nanocolumns elongated along the growth axis and their diameter is

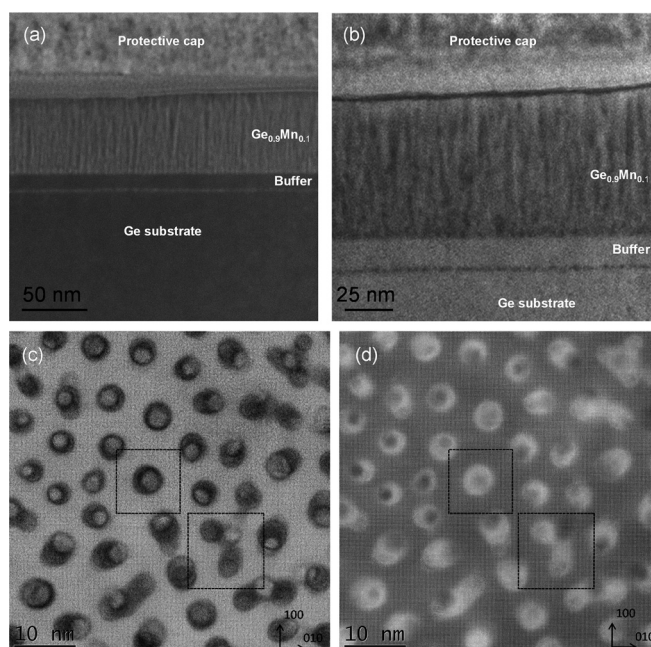


FIG. 1. Cross section TEM views of the $\text{Ge}_{0.9}\text{Mn}_{0.1}$ thin film: (a) STEM-LAADF mode, (b) classical TEM mode, and high resolution observations in plane view of the Mn-rich nanocolumns: (c) BF image acquired with a collection angle of 0 to 10.5 mrad. (d) ADF image of the same area acquired simultaneously with a collection angle of 44 to 110 mrad.

$\sim 3\text{ nm}$. The interface between the Ge buffer layer and the $\text{Ge}_{0.9}\text{Mn}_{0.1}$ is flat.

The nanostructures observed in HRTEM were characterized by atom probe tomography. Figure 3 represents the mass spectrum obtained after atom probe analyses of the $\text{Ge}_{0.9}\text{Mn}_{0.1}$ thin film. The single isotope of Mn and the five

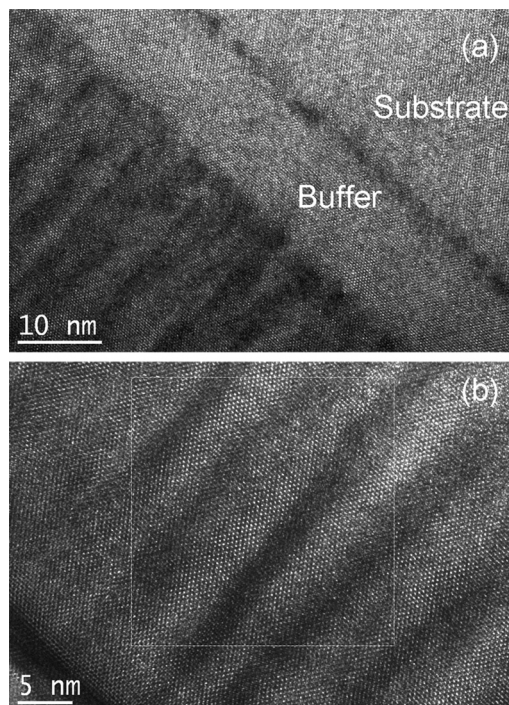


FIG. 2. Cross section TEM views of the $\text{Ge}_{0.9}\text{Mn}_{0.1}$ thin film in high resolution mode: (a) image of the interface between the Ge buffer layer and the $\text{Ge}_{0.9}\text{Mn}_{0.1}$ film. (b) Image of the $\text{Ge}_{0.9}\text{Mn}_{0.1}$ layer; the nanocolumns are clearly observed.

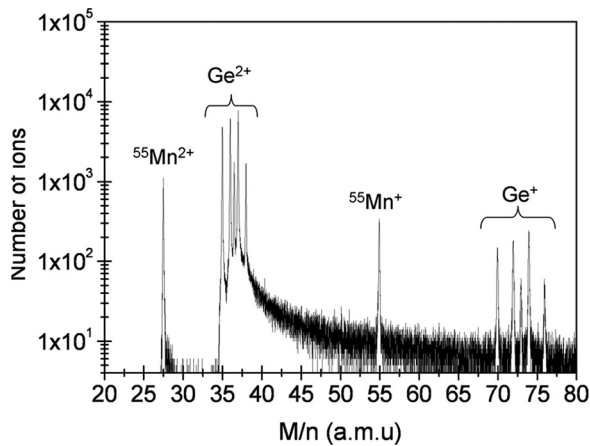


FIG. 3. Mass spectrum of the $\text{Ge}_{0.9}\text{Mn}_{0.1}$ thin film obtained by LAWATAP ($\lambda = 342$ nm).

isotopes of Ge are clearly visible. The atomic-scale reconstruction of the $\text{Ge}_{0.9}\text{Mn}_{0.1}$ film in 3D is plotted in Figure 4. Note that each dot represents one Ge or Mn atom. It clearly shows the 3D inhomogeneous distribution of Mn atoms within the Ge matrix. They form nanocolumns along the growth axis in the whole thickness of the $\text{Ge}_{0.9}\text{Mn}_{0.1}$ thin film. Their diameters range between 2.5 and 3 nm and their average distance is of about 5 nm. The quasi-periodicity of the nanocolumns observed is an intriguing issue. The latter could originate from the overlap of elastic coherency stress fields generated by the lattice misfit between (coherent) nanocolumns and the surrounding matrix.

This result confirms that Mn atoms tend to segregate during the growth of the layer as a consequence of the almost null solubility limit of Mn in Ge. Note that most of the nanocolumns display a rippled aspect and are regularly distributed in the layer volume with a characteristic spacing of around 3 to 4 nm. This spacing is in agreement with TEM observations. APT measurements also show that a significant number of nanocolumns do not extend over the whole thickness of the

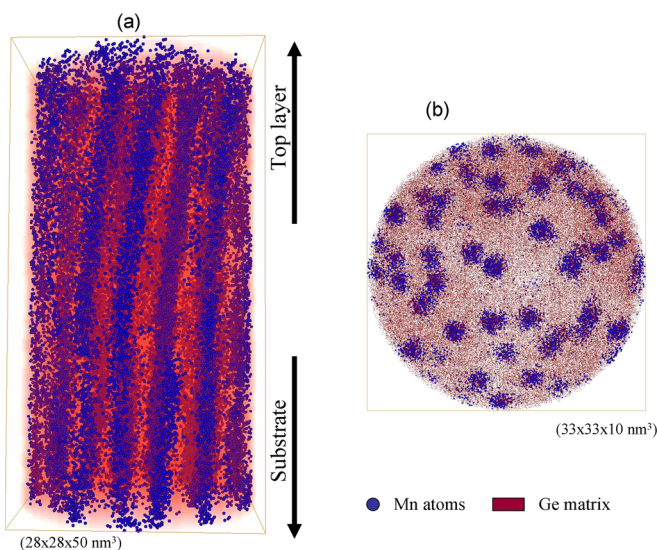


FIG. 4. 3D images of Mn-rich nanocolumns embedded in the Ge matrix obtained by atom probe tomography. (a) Side view, (b) top view. The Mn atoms and the Ge matrix are represented in blue and red, respectively.

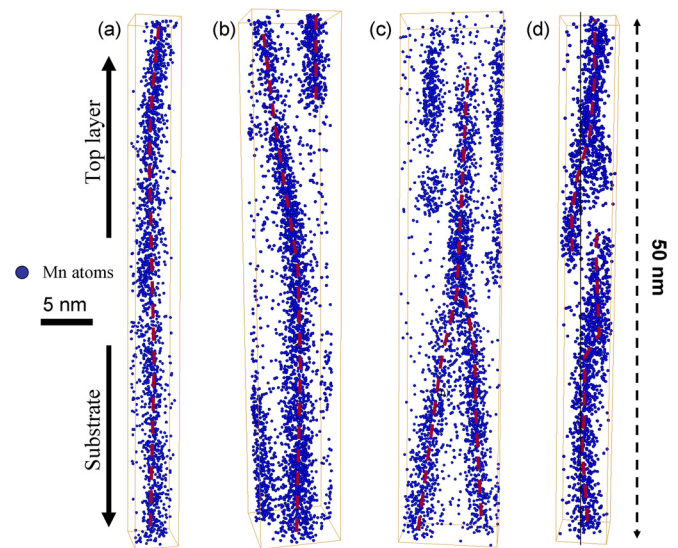


FIG. 5. 3D images of single Mn-rich nanocolumns (only the Mn are represented for clarity). (a) Continuous nanocolumn, (b) curved nanocolumn correlated to the nucleation and growth of another nanocolumn, (c) junctions between bent nanocolumns followed by an interruption, (d) discontinuous nanocolumn.

$\text{Ge}_{0.9}\text{Mn}_{0.1}$ film. Figure 5 shows characteristic morphologies of the Mn-rich nanocolumns observed in the reconstructed volume. Indeed, continuous (Fig. 5(a)) and interrupted or discontinuous columns are observed (Figs. 5(c) and 5(d)). Curved columns, new nucleation within the layer and junctions between bent nanocolumns are also observed (Figs. 5(b) and 5(c)). This bending is very likely related to the growth process of the nanocolumns which can be influenced by the roughness of the substrate surface.²⁶

Similar features are also observed from the STEM plane view images of Figures 1(c) and 1(d). It appears that the projections of the columns are not identical but rather show various shapes. The zoom captures in Figure 6 show for instance two kinds of nanocolumns exhibiting straight shape (Figs. 6(a) and 6(b)) probably similar to the one shown on Figure 5(a), and Y shape (Figs. 6(c) and 6(d)) with only two branches emerging on the top surface which correspond to the reversed geometry of Figure 5(c). In this latter case, the main branch stops within the volume and does not emerge. As a consequence its contrast is lower on the STEM image.

Figure 7 shows an APT-3D image of the interface between the Ge buffer layer and the $\text{Ge}_{0.9}\text{Mn}_{0.1}$ thin film. The cross section of 2 nm thick is taken in this volume (Fig. 7(b)) and confirms that the interface is well defined and flat. Once again interrupted columns are observed. These APT observations show that not all the nanocolumns are identical in shape and length. More interesting are the chemical measurements showing that the matrix contains a very small amount of Mn (smaller than the background noise level of the APT: $\sim 0.05\%$) in accordance with the almost null solubility of Mn in the diamond structure of Ge. Mn atoms are exclusively located in the nanocolumns. This means that during the deposition process, Mn atoms rapidly migrate (surface diffusion) in order to form Mn-enriched nuclei. In proportion as Ge and Mn atoms are co-deposited, one assists to the axial growth of Mn-enriched nuclei perpendicular to the substrate surface.

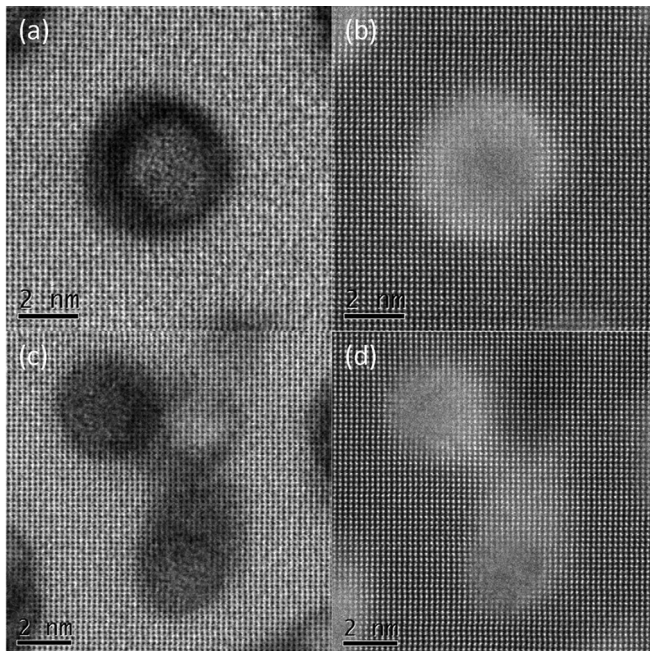


FIG. 6. Zoom of Figures 1(c) and 1(d) (the zoomed area are indicated by square): (a) and (b) BF and ADF images, respectively, of the same emerging nanocolumns with a straight shape. (c) and (d) BF and ADF images, respectively, of other nanocolumns exhibiting a Y shape with two emerging branches and a nonemerging central-one.

Due to both, the very large driving force for nucleation (very high Mn amount compared to solubility) and the very high surface mobility of Mn atoms even at the low temperature (100 °C, temperature at which the MBE was performed), Mn nanocolumns rapidly grow leading to an almost complete Mn depletion in the remaining Ge phase.

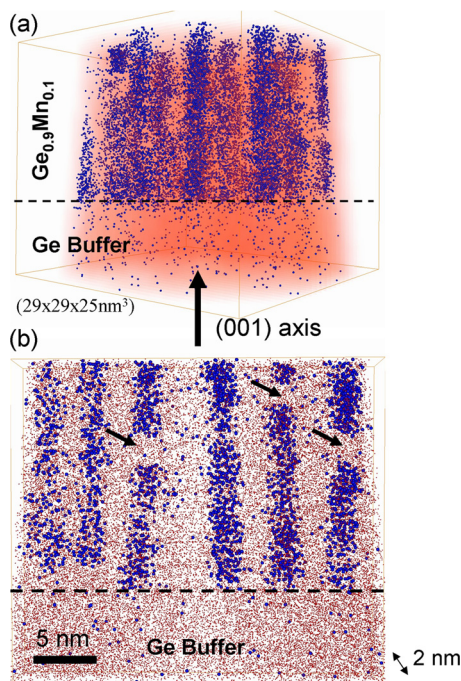


FIG. 7. (a) 3D images of the interface between the Ge buffer layer and the $\text{Ge}_{0.9}\text{Mn}_{0.1}$ thin film. (b) Slice of 2 nm thick taken in the 3D volume showing the interface between the Ge buffer layer and the $\text{Ge}_{0.9}\text{Mn}_{0.1}$ thin film; black arrows indicate the interruption of some nanocolumns. The Mn atoms and the Ge matrix are represented in blue and red, respectively.

The chemical composition of the nanocolumns as derived from APT investigations was carefully assessed. It is well known that the analysis of samples composed of phases with distinct evaporation fields may lead to biased composition data.²⁷ Careful examination of atomic maps demonstrates that the apparent atomic density (at./nm^3) in the Mn-rich regions (Fig. 4(b)) was much larger than the surrounding Ge phase. This confirms that Mn-rich nanocolumns have a lower evaporation field than Ge. Lower field Mn-rich regions exhibit larger curvatures at the tip surface. This focuses the effects of ion trajectories that give rise to apparent higher atomic densities in Mn-rich regions from the APT reconstructions. In addition to possible overlap of ions trajectories, these local magnification effects result from the close vicinity of nanocolumns-Ge interfaces. Ge ions coming from the surrounding matrix may therefore fall in the Mn enriched region (Fig. 4(b)) then leading to an overestimation of the atomic fraction of Ge in the nanocolumns or equivalently to an underestimation of the atomic fraction of Mn in the nanocolumns. We note that the smaller the precipitates (here the nanocolumns), the larger the composition bias.

The composition of a series of nanocolumns was thus measured and corrected using the model of Blavette *et al.*²⁸ Similar corrections were done following Talbot *et al.*²⁹ The corrected atomic fraction in the nanocolumns was almost 50% larger than that measured. The corrected Mn content in the nanocolumns ranged from 25% to 35% with a mean value of 30%. It is worth mentioning that apparent solute content is expected to increase with increasing sizes (i.e., decrease of the influence of trajectory overlaps, lower bias). No correlation between the corrected Mn content and the nanocolumns radius was evidenced (Fig. 8), suggesting that our corrections are reliable. In addition, corrected APT data (30 at. %) are in fair agreement with previous TEM-EELS measurements (30 at. % to 38 at. %).¹¹ The molar fraction (close to the volume fraction if the nanocolumns are considered with the same structure as Ge) of Mn-enriched magnetic phase as derived by the lever rule was $f = C_0/C_\beta \sim 20\%$ (with C_0 the nominal composition of the layer equal to 6% as measured by APT, and C_β the mean composition of the nanocolumns equal to 30 at%). It is interesting to compare this latter value to the volume fraction f_v derived from the microstructure features of Fig. 4. Around 42 nanocolumns ($n = 42$) are observed in this figure ($33 \times 33 \text{ nm}^2$), leading to a mean spacing $d \sim \sqrt{S/n}$

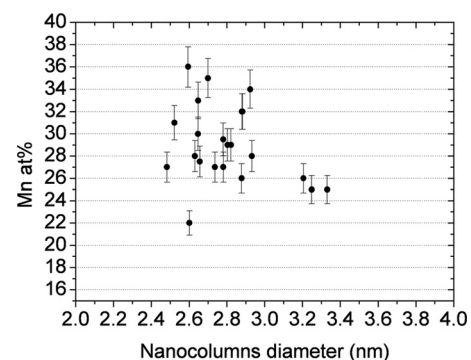


FIG. 8. Mn content in at. % of the nanocolumns as a function of the nanocolumns diameter.

close to 5 nm and a volume fraction $f_v \sim \pi\Phi^2/(4d^2) \sim 23\%$. This value of f_v is very close to that derived from the phase composition (lever rule). This is an additional argument in favour of the reliability of the present composition measurements and that consolidates the corrected amount of Mn in nanocolumns (i.e., 30 at. %).

Mn levels in the nanocolumns, close to 30 at. %, are much smaller than those in the expected equilibrium phases (57.9 at. % for $\text{Ge}_8\text{Mn}_{11}$ or 62.5 at. % of Mn Ge_3Mn_5). This raises the important question of the decomposition mechanism and of the kinetic pathway as well. The nucleation of the nanocolumns with a low Mn content compared to the equilibrium phases is expected for highly supersaturated systems.^{30,31} Non-classical theories of nucleation, which rely on the minimisation of the nucleation barrier (that is a function of the driving force, the interfacial and elastic energies), indeed predict that nuclei may have a smaller solute content and diffuse interfaces.³¹ 2D spinodal decomposition was also postulated in this system and in other DMS ((Ga,Mn)As).^{32,33} Spinodal decomposition proceeds via the amplification of concentration fluctuations with increasing amplitudes. Because of the very high supersaturation, it is likely that the Mn concentration exceeds the spinodal limit. The system may therefore enter in an unstable regime (versus a metastable regime for nucleation and growth) and decompose spinodally. In addition to such thermodynamics arguments, kinetics effects related to diffusion may also account for this low content in the nanocolumns.

Corrected concentration profiles across the nanocolumns were also performed. Figure 9 shows two concentration profiles taken from two distinct heights in the same column. The core concentration along a single object varies from 35 at. % (profile 1) to 50 at. % (profile 2). These results, which could not be accessed by EELS experiments, indicate that chemical variations also occur along the growth axis.

B. Magnetic properties

SQUID measurements were performed in order to investigate the magnetic properties of the $\text{Ge}_{0.9}\text{Mn}_{0.1}$ thin film. The magnetic field was applied in the sample plane. Hysteresis loops, temperature-dependent magnetization in zero-field cooled (ZFC) and field cooled (FC) conditions, and temperature-dependent magnetization at 5 Tesla (M_{5T}) are shown in Figures 10(a)–10(c), respectively. The hysteresis loops exhibit a ferromagnetic behaviour at 5 K characterized

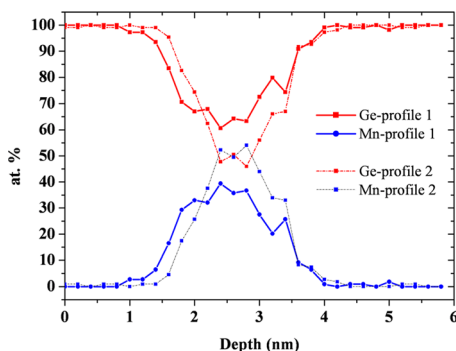


FIG. 9. Corrected concentration profiles taken across a single Mn-rich nanocolumn at two different heights.

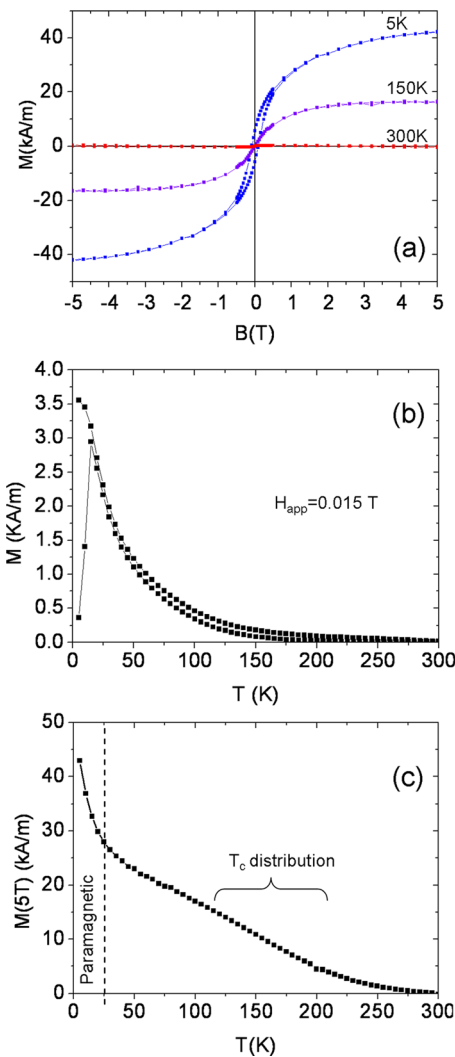


FIG. 10. (a) Hysteresis loops $M(H)$ at 5, 150, and 300 K. (b) ZFC/FC measurements recorded with a field of 0.015 T. (c) Temperature dependence of the magnetization at 5 T (M_{5T}). The magnetic field was applied in the film plane.

by a coercive field $\mu_0 H_c = 0.09$ T and a remanent magnetization M_R equal to 5.8 kA m^{-1} . $\mu_0 H_c$ and M_R vanish and the magnetization curves exhibit a pronounced S-shape when the temperature is increased. We do not see a clear difference between in-plane and out-of-plane magnetic measurements (not shown). It mainly arises from shape anisotropy: the magnetization lies along the columns axis. However, due to the very low value of M_S , this shape anisotropy is very small. Only electron paramagnetic resonance (EPR) measurements could give us an estimation of it.¹⁷ When nanocolumns are crystalline, it is also possible to measure an in-plane four-fold magnetic anisotropy due to cubic anisotropy.¹⁷ The shape of the ZFC/FC curves (Fig. 10(b)) is typically observed in superparamagnetic (SPM) particle assemblies with a narrow size distribution. The M_{ZFC} curve exhibits a narrow peak (which reflects the size dispersion) with a maximum temperature T_{max} around 15 K and a quasi perfect overlapping with the M_{FC} curve above T_{max} . Note that T_{max} is usually considered as the blocking temperature. The $1/T$ decrease of the magnetization is a typical signature of superparamagnetism. This is in good agreement with the temperature dependence of

magnetization curves plotted in Fig. 10(a). The $M_{5T}(T)$ curve in Fig. 10(c) gives more precisions about the magnetic behaviour of the $\text{Ge}_{0.9}\text{Mn}_{0.1}$ thin film. It displays two distinct contributions: a paramagnetic contribution at very low temperature as shown in Figure 10(c) and a ferromagnetic contribution which does not exhibit a precise Curie temperature (T_C) suggesting a T_C distribution with a mean value around 150 K. Based on the previous studies and on the results obtained by atom probe tomography, we can attribute the magnetic properties of the $\text{Ge}_{0.9}\text{Mn}_{0.1}$ thin film to the nanocolumns embedded in the Ge matrix. In the previous studies, from EELS measurements, we raised the hypothesis that diluted Mn atoms in the Ge matrix (<1 at. %) give the paramagnetic signal observed at low temperature in the $M_{5T}(T)$ curve.¹¹ The more resolved APT and its ability to perform 3D images allows us to revise this initial hypothesis. It allows us to clearly rule out diluted Mn atoms in the Ge matrix as the origin of this low temperature paramagnetic signal. Taking into account the variation of Mn content in the nanocolumns, we may now infer that this paramagnetic signal rather comes from fragments of nanocolumns in which the Mn concentration is reduced down to the limit where Mn atoms are paramagnetic. The T_C distribution observed in Figure 10(c) may be also correlated to the Mn content fluctuation in the nanocolumns. Thus the nanocolumns seem to be composed of different regions with different Mn content which lead to the appearance of two distinct magnetic phases: a paramagnetic phase and a ferromagnetic one. Moreover, the small diameter of the nanocolumns gives rise to the superparamagnetic behaviour of the ferromagnetic phase above ~ 15 K. At 300 K, the nanocolumns are all paramagnetic.

IV. CONCLUSION

HRTEM and HRSTEM coupled with APT measurements were used as complementary technique to characterize self-organised Mn-rich nanocolumns embedded in a Ge matrix. Thanks to the 3D imaging capability of APT and its high spatial resolution, a precise characterization of Mn-rich nanocolumns was provided. Subsequent new and refined correlations to the magnetic properties were suggested. The morphology and the local chemical compositions of nanocolumns were characterized and new features were revealed. It was confirmed that Mn-rich nanocolumns along the growth axis with a diameter of ~ 3 nm are regularly dispersed in the Ge matrix. Curved, interrupted, bent and joint nanocolumns were additionally evidenced. It was also highlighted that nanocolumns can nucleate within the $\text{Ge}_{0.9}\text{Mn}_{0.1}$ thin film and not necessarily at the interface with the Ge buffer layer. Quantitatively, it was shown that the Mn content of the nanocolumns ranges between 25% and 35% with a mean value of about 30%. In addition, the APT technique allowed us to measure that the nanocolumns exhibit chemical fluctuations along the growth direction. It was also found that, contrary to previous experiments with lower resolution, the remaining matrix is composed of almost pure Ge (<0.05% of Mn). These findings constituted important information in order to definitely conclude on the various origins of the magnetic contributions of the film. At 300 K, the nanocolumns exhibited

a paramagnetic behaviour. At lower temperature, two magnetic phases were observed. The first one is a paramagnetic phase that can now be, in the light of the present ATP observations, attributed to fragments of nanocolumns with a low Mn content. The second one is a ferromagnetic phase exhibiting a T_C distribution. In view of the present study, we can infer that this latter distribution likely originates from the variation of the Mn content in the nanocolumns. Furthermore, the small diameter and low shape anisotropy (due to the low saturation magnetization) of the nanocolumns certainly leads to the occurrence of the superparamagnetic relaxations of the ferromagnetic regions.

A deeper understanding of atomic-scale mechanisms beneath the formation of such self-organised nanostructures is a key issue both from a fundamental point of view but also to produce magnetic semiconductors with advanced properties. This evidently raises the problem of the crystallographic structure of Mn-enriched nanocolumns. It is well known that coherent nucleation (i.e., nuclei with the same structure as the Ge-substrate and/or the surrounding Ge phase) is much easier than the nucleation of noniso-structural phases. Consequently, we would expect that the nanocolumns have the diamond structure of Ge or a neighbour structure. Resolving unambiguously, the structure of such small nanocolumns using TEM is far from trivial. Further investigations are needed. More generally, the kinetic pathway of formation of such nanostructures (non-classical nucleation? Spinodal decomposition?) during the deposit process is a very exciting issue but dealing with this at the atomic scale is also a great challenge. Further experiments related to the growth kinetics are planned and simulations based on rigid lattice Kinetic Monte-Carlo are in progress.

ACKNOWLEDGMENTS

V. Baltz, P. Bayle-guillemaud, E. Prestat, A. Barski, and M. Jamet would like to acknowledge the financial support from the agence nationale de la recherche (French ANR project GEMO) and the nanoscience foundation of Grenoble (RTRA project IMAGE). F. Hue is also acknowledged for fruitful discussions.

¹H. Ohno, *Science* **281**, 951 (1998).

²J. K. Furdyna, *J. Appl. Phys.* **64**, R29 (1988).

³S. B. Ogale, *Adv. Mater.* **22**, 3125 (2010).

⁴T. Dietl, *Physica E* **35**, 293 (2006).

⁵T. Dietl, *J. Appl. Phys.* **103**, 07D111 (2008).

⁶N. Samarth, S. Chun, K. Ku, S. Potashnik, and P. Schiffer, *Solid State Commun.* **127**, 173 (2003).

⁷P. N. Hai, M. Yokoyama, S. Ohya, and M. Tanaka, *Physica E* **32**, 416 (2006).

⁸Y. D. Park, A. T. Hanbicki, S. C. Erwin, C. S. Hellberg, J. M. Sullivan, J. E. Mattson, T. F. Ambrose, A. Wilson, G. Spanos, and B. T. Jonker, *Science* **295**, 651 (2002).

⁹S. Ahlers, D. Bougeard, N. Sircar, G. Abstreiter, A. Trampert, M. Opel, and R. Gross, *Phys. Rev. B* **74**, 214411 (2006).

¹⁰D. Bougeard, S. Ahlers, A. Trampert, N. Sircar, and G. Abstreiter, *Phys. Rev. Lett.* **97**, 237202 (2006).

¹¹T. Devillers, M. Jamet, A. Barski, V. Poydenot, P. Bayle-Guillemaud, E. Bellet-Amalric, S. Cherifi, and J. Cibert, *Phys. Rev. B* **76**, 205306 (2007).

¹²S. Tardif, I.-S. Yu, T. Devillers, M. Jamet, S. Cherifi, J. Cibert, A. Barski, P. Bayle-Guillemaud, and E. Bellet-Amalric, *Spintronics* **7036**, 703615 (2008).

- ¹³D. Bougeard, N. Sircar, S. Ahlers, V. Lang, G. Abstreiter, A. Trampert, J. M. LeBeau, S. Stemmer, D. W. Saxe, and A. Cerezo, *Nano Lett.* **9**, 3743 (2009).
- ¹⁴R. Reiley, D. Perea, L. He, F. Tsui, and L. Lauhon, *J. Phys. Chem.* **116**, 276 (2012).
- ¹⁵Y. Wang, F. Xiu, J. Zou, K. L. Wang, and A. P. Jacob, *Appl. Phys. Lett.* **96**, 051905 (2010).
- ¹⁶Y. Wang, F. Xiu, Y. Wang, J. Zou, W. Beyermann, Y. Zhou, and K. Wang, *Nanoscale Res. Lett.* **6**, 134 (2011).
- ¹⁷A. Jain, M. Jamet, A. Barski, T. Devillers, C. Porret, P. Bayle-Guillemaud, S. Gambarelli, V. Maurel, and G. Desfonds, *Appl. Phys. Lett.* **97**, 202502 (2010).
- ¹⁸D. Blavette, T. Al Kassab, E. Cadel, A. Mackel, F. Vurpillot, M. Gilbert, O. Cojocar, and B. Deconihout, *Int. J. Mater. Res.* **99**, 454 (2008).
- ¹⁹M. K. Miller and R. G. Forbes, *Mater. Charact.* **60**, 461 (2009).
- ²⁰M. Kodzuka, T. Ohkubo, K. Hono, F. Matsukura, and H. Ohno, *Ultramicroscopy* **109**, 644 (2009).
- ²¹D. J. Payne and E. A. Marquis, *Chem. Mater.* **23**, 1085 (2011).
- ²²R. Lardé, E. Talbot, P. Pareige, H. Bieber, G. Schmerber, S. Colis, V. Pierron-Bohnes, and A. Dinia, *J. Am. Chem. Soc.* **133**, 1451 (2011).
- ²³R. Lardé, E. Talbot, F. Vurpillot, P. Pareige, G. Schmerber, E. Beaupaire, A. Dinia, and V. Pierron-Bohnes, *J. Appl. Phys.* **105**, 126107 (2009).
- ²⁴L. Li, Y. Guo, X. Y. Cui, R. Zheng, K. Ohtani, C. Kong, A. V. Ceguerra, M. P. Moody, J. D. Ye, H. H. Tan, C. Jagadish, H. Liu, C. Stampfl, H. Ohno, S. P. Ringer, and F. Matsukura, *Phys. Rev. B* **85**, 174430 (2012).
- ²⁵K. Thompson, D. Lawrence, D. J. Larson, J. D. Olson, T. F. Kelly, and B. Gorman, *Ultramicroscopy* **107**, 131 (2007).
- ²⁶I.-S. Yu, M. Jamet, T. Devillers, A. Barski, P. Bayle-Guillemaud, C. Beigné, J. Rothman, V. Baltz, and J. Cibert, *Phys. Rev. B* **82**, 035308 (2010).
- ²⁷F. Vurpillot, A. Bostel, and D. Blavette, *Appl. Phys. Lett.* **76**, 3127 (2000).
- ²⁸D. Blavette, F. Vurpillot, P. Pareige, and A. Menand, *Ultramicroscopy* **89**, 145 (2001).
- ²⁹E. Talbot, R. Lardé, F. Gourbilleau, C. Dufour, and P. Pareige, *Eur. Phys. Lett.* **87**, 26004 (2009).
- ³⁰J. W. P. Schmelzer, J. Schmelzer, and I. Gutzow, *J. Chem. Phys.* **112**, 3820 (2000).
- ³¹T. Philippe and D. Blavette, *Philos. Mag.* **91**, 4606 (2011).
- ³²K. Sato, T. Fukushima, and H. Katayama-Yoshida, *J. Phys.: Condens. Matter* **19**, 365212 (2007).
- ³³T. Fukushima, K. Sato, H. Katayama-Yoshida, and P. H. Dederichs, *Jpn. J. Appl. Phys., Part 2* **45**, L416 (2006).